Plasma Chemistry and Plasma Processing, Vol. 22, No. 1, March 2002 (© 2002)

Dynamics of Splat Formation in Plasma Spray Coating Process

Javad Mostaghimi,[1,2] Mohammad Pasandideh-Fard,[1] and Sanjeev Chandra[1]

Received January 9, 2001; revised April 4, 2001

The paper describes recent developments in modeling formation of plasma spray coatings. Specific attention is paid to the three-dimensional simulation of droplet impact and solidification under plasma spraying conditions. It is shown that the extent of maximum spread is primarily determined by the Reynolds number and, to a lesser degree, by the Weber number. Splashing and break-up is shown to be the result of solidification; fluid instabilities do not play a significant role in this regard. Finally, the effect of solidification on droplet spreading is insignificant when the ratio of Stefan number to Prandtl number is much smaller than unity.

KEY WORDS: Plasma spraying; splat formation; 3-D simulation.

1. INTRODUCTION

Plasma spray coating is a process by which the high temperature of a plasma is employed to melt powders of metallic or non-metallic materials and spray them onto a substrate, forming a dense deposit. The process is commonly used to apply protective coatings on components to shield them from wear, corrosion, and high temperatures. Both direct current plasma (dc), and—to a lesser degree—radio frequency inductively coupled plasma (rf-ICP) are employed as the heat source for melting and accelerating the powders. The process may be at atmospheric pressure or under vacuum. Figure 1 shows a schematic diagram of the atmospheric dc plasma spray coating process.

Plasma coatings are built up by agglomeration of splats formed by the impact, spread, and solidification of individual particles. Figure 2 shows a

[1]Centre for Advanced Coating Technologies, Department of Mechanical and Industrial Engineering, University of Toronto, Toronto, Ontario, Canada M5S-3G8.
[2]To whom all correspondence should be addressed.

0272-4324/02/0300-0059/0 © 2002 Plenum Publishing Corporation

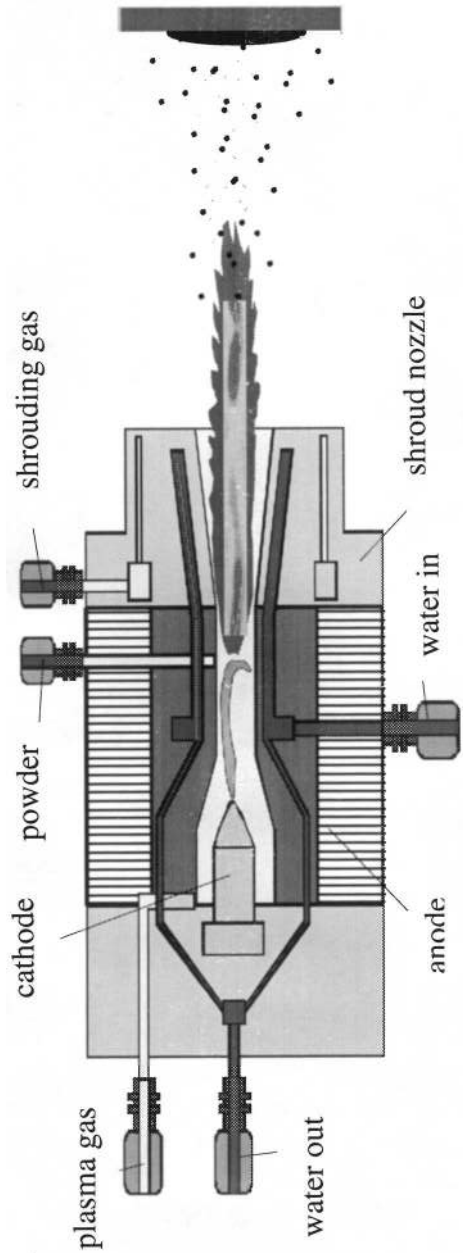

Fig. 1. Schematic of a dc plasma spray coating process.

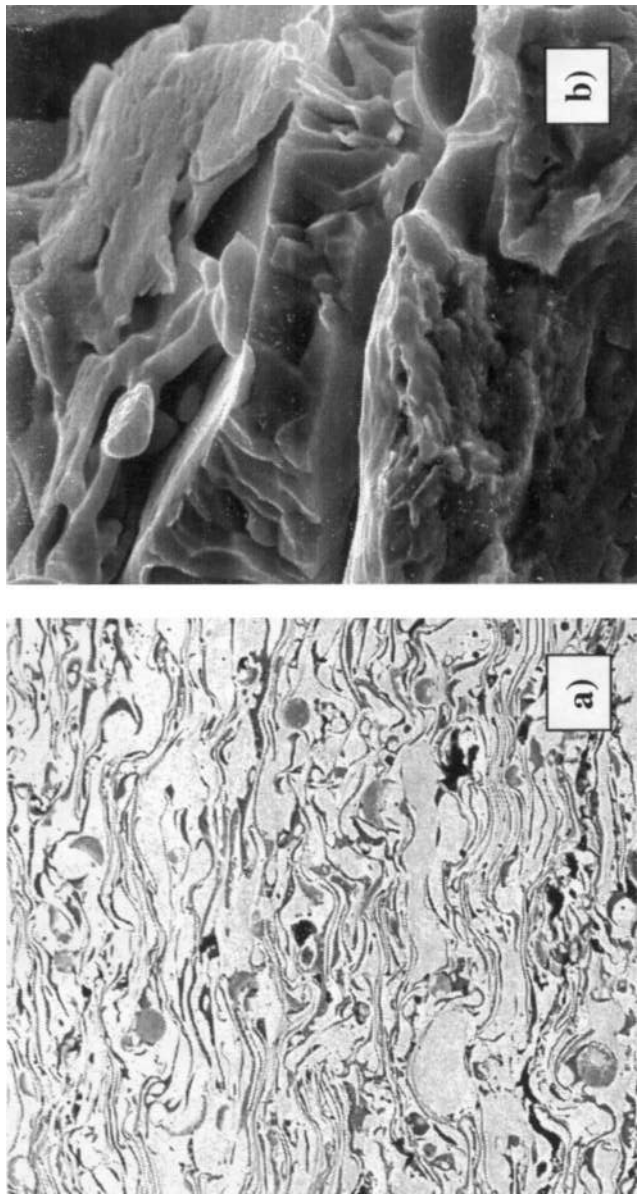

Fig. 2. A typical cross section of nickel sprayed plasma coating (a), with higher magnification (b).

typical cross-section of dc plasma sprayed nickel coating. The state of particles at the point of impact is dependent on their trajectory and residence time within the plasma. Thus, the particles may be fully or partially melted and few particles may be in solid form. Coating properties such as porosity, adhesion strength, and surface roughness depend on the shape of these splats and how they bond together and to the substrate. The splat shape is dependent on material properties of the powder; impact conditions, e.g., impact velocity and temperature; and substrate conditions, e.g., substrate topology and temperature.

Understanding the dependence of the microstructure of spray coatings on operating conditions of the plasma spray system is of great practical interest. To obtain good quality coatings the spray parameters must be selected carefully, and due to the large variety in process parameters, much trial and error goes into optimizing the process for each specific coating and substrate combinations. A great deal of research is currently devoted to exactly understand how varying spray parameters changes coating properties. Mathematical modeling of the process can play a significant role in reducing the extent of such trial and error procedures.

A complete mathematical model of dc plasma spraying systems involves three distinct regions (see Fig. 1):

(i) Plasma generation zone;
(ii) particle heating zone; and
(iii) deposition zone.

The particle-heating region has been the subject of considerable theoretical research over the last 20 years. In particular, the pioneering work of Lee and Pfender[1] is of great importance. In contrast, modeling of plasma generation zone and deposition zone has not advanced enough and considerable research is still needed. In this paper we describe recent advances in modeling the deposition zone.

2. DROPLET IMPACT AND SOLIDIFICATION

Formation of coatings is a stochastic process in which particles with certain size, velocity, and temperature distributions impact on a substrate. Currently, efforts are underway to predict microstructure of coatings by employing the Monte Carlo simulation technique. The model assumes a normal distribution for all the relevant variables as well as specification of the spray gun movement.[2] One of the most important features in stochastic modeling of the coating formation is the shape of individual splats as a function of particle impact conditions and the substrate temperature and

topology. We expect a model of splat formation can answer the following questions:

1. What is the relationship between the final splat shape and impact parameters, powder and substrate properties, and substrate roughness?
2. What causes splashing and break-up?
3. How do splats interact?

Prediction of splat shapes involves numerical simulation of fluid flow and heat transfer of an impacting droplet. In general, this is a three-dimensional, time-dependent problem. One challenge—specific to this problem—is the prediction of rapid and large deformation of the impacting droplet surface. In what follows, we describe the current state of modeling droplet impact and solidification.

2.1. Axi-Symmetric Input

Before we describe the details of the 3-D mathematical model, let us describe the most important variables that control the impact phenomenon. Consider the isothermal normal impact of a spherical droplet on a smooth, flat surface, as shown in Fig. 3. Furthermore, assume the gas phase does not influence the impact. The parameters that influence such impact include: initial droplet diameter D_0, impact velocity V_0, liquid density ρ, liquid viscosity μ, liquid–gas surface tension γ, and liquid–solid contact angle θ. Nondimensionalization of the problem reduces the number of variables to three. These are the contact angle, the Reynolds and the Weber numbers, defined below:

$$\mathrm{Re} = \frac{\rho V_0 D_0}{\mu}; \qquad \mathrm{We} = \frac{\rho V_0^2 D_0}{\gamma} \tag{1}$$

Re is a measure of the droplet inertia to viscous force and We is a measure of inertia to the surface tension force. There has been many successful

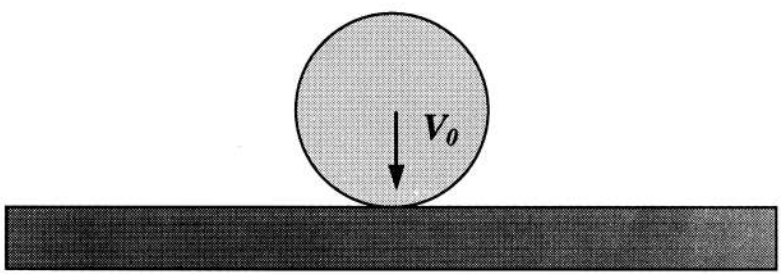

Fig. 3. Schematic of droplet just before impact.

attempts to derive analytical expressions for the extent of maximum spread, $\xi_{max} = D_{max}/D_0$, as a function of process variables.[3–5] For example, Pasandideh-Fard *et al.*[5] showed that the maximum spread can be expressed as

$$\xi_{max} = \frac{D_{max}}{D_0} = \sqrt{\frac{We + 12}{3(1 - \cos\theta_a) + 4(We/\sqrt{Re})}} \tag{2}$$

For thermal spray conditions, the first term in the denominator is negligible compared to the second term; furthermore, typically, $We \gg 12$ resulting in the following simple relation for the maximum spread

$$\xi_{max} = 0.5\,Re^{0.25} \tag{3}$$

Typical values for maximum spread factor in plasma spray process are in the range of 3 to 6. Analytical relations were also obtained that considered the effect of solidification on the maximum spread[6]

$$\xi_{max} = \sqrt{\frac{We + 12}{3(1 - \cos\theta) + 4(We/\sqrt{Re}) + We\sqrt{(3Ste)/(4Pe)}}} \tag{4}$$

where $Ste = C(T_m - T_{w,i})/H_f$ is the Stefan number, C is droplet heat capacity, T_m is droplet melting temperature and $T_{w,i}$ is the initial substrate temperature; $Pr = \nu/\alpha$ is the droplet Prandtl number, ν and α are droplet kinematic viscosity and thermal diffusivity, respectively. The effect of solidification is to reduce the degree of maximum spread. The degree of reduction is dependent upon the ratio of Stefan and Prandtl numbers.

The above relations are quite useful in partially providing the answer to the first question; i.e., what is the relation between maximum spread and impact variables. Because of many simplifications in their derivation, their usefulness is, however, limited.

To better understand the dynamics of impact, spread, and solidification, a number of two-dimensional, axi-symmetric models were developed over the last ten years. Zhao *et al.*[7,8] studied, both experimentally and numerically, heat transfer and fluid flow of an impacting droplet. Solidification was not considered in this work. Bennet and Poulikakos[9] and Kang *et al.*[10] studied droplet deposition assuming solidification to start after spreading is completed. As discussed above, the validity of this assumption depends on both Prandtl and Stefan numbers. Liu *et al.*,[11] Bertagnolli *et al.*,[12] and Trapaga *et al.*[13] used finite difference techniques to study solidification and spreading of the impacting drops. The substrate was, however, assumed to be isothermal. Furthermore, the important effect of thermal contact resistance between the drop and the substrate was not considered. In these studies, the liquid–solid contact angle was considered to be constant, with an arbitrarily assigned value. Pasandideh-Fard *et al.*,[5] however,

showed that the value of contact angle can have a significant effect on the results.

Pasandideh-Fard and Mostaghimi[14] studied the effect of thermal contact resistance between the droplet and the substrate. They showed that its magnitude could have a dramatic effect on droplet spreading and solidification. Solidification and heat transfer within the substrate was modeled assuming one-dimensional heat conduction. The model was later completed and a fully two-dimensional axi-symmetric model of droplet impact was developed[6] and impact and solidification of relatively large tin droplets (~2 mm diameter) on stainless steel substrates were studied both numerically and experimentally. The model correctly predicted the shape of the deforming droplet. The values of thermal contact resistance were estimated by matching the numerical predictions of substrate temperature with those measured experimentally. While thermal contact resistance should, in principle, vary at different contact points, it was shown that accurate simulations of the impact could be done using a constant value. The results also showed the sensitivity of the predicted maximum spread to the value of thermal contact resistance.

A few experimental studies have investigated impact of molten droplets. Madejski[3,4] developed a simple model to predict the maximum splat diameter of a droplet after impact, and compared his predictions with the size of alumina droplets deposited on a cold surface. Inada[15] measured the temperature variation of a plate on which a molten lead droplet was dropped, and noted that the droplet cooling rate was a function of impact velocity. Watanabe *et al.*[16] photographed impact of *n*-cetane and *n*-eicosane droplets on a cold surface and concluded that in their tests droplets spread completely before solidifying. Fukanuma and Ohmori[17] photographed the impact of tin and zinc droplets and also found that freezing had no influence on droplet spread. Inada and Yang[18] used holographic interferometry to observe droplet-substrate contact during impact of lead droplets on a quartz plate. Liu *et al.*[19] measured the temperature variation on the upper surface of an impacting metal droplet by a pyrometer, and used these results to estimate the thermal resistance under the drop. However, the response time of the pyrometer (25 ms) was longer than the time taken by the droplet to spread, so that their results are applicable to the period after the droplet had come to rest rather than the duration of the impact itself. Pasandideh-Fard *et al.*[6] photographed the impact of tin droplets on stainless steel substrate and measured the changes in substrate temperature during the impact. They showed that the value of the maximum spread is sensitive to the magnitude of thermal contact resistance, which in their case was estimated from the measurements.

2.2. Splashing and Break-up

Two-dimensional models have been very useful in showing the dynamics of impact and solidification under limited conditions. In reality, the majority of impacts occur under conditions that are not axi-symmetric. Even under axi-symmetric impact conditions, the contact line may become unstable; fingers develop and grow and may eventually break away from the bulk of the splat.

The first experimental study of droplet fingering and splashing—in the absence of solidification—was that of Worthington[20,21] which was published over a century ago. Worthington observed that the number of fingers increased with droplet size and impact speed; observed merging of the fingers at or soon after the maximum spread; and found fingering to be more pronounced for fluids that did not wet the substrate. Many researchers have since contributed to the understanding of the fingering and splashing in the absence of solidification. A review of their findings may be found in the recent works of Bussmann *et al.*[22,23]

Bussmann *et al.*[22–24] developed a three-dimensional model for the isothermal impact of a droplet on a solid surface. The model was based on the extension of the two-dimensional RIPPLE[25] algorithm to three dimensions. The model employs a fixed-grid Eulerian approach along with a volume tracking algorithm to track fluid deformation and droplet free surface. The choice of fixed-grid technique is attractive for several reasons: it is relatively simple to implement; volume tracking method is capable to model gross fluid deformation, including breakup; and the relatively small demand on computational resources.

Pasandideh-Fard *et al.*[26,27] extended the three-dimensional model of Bussmann *et al.* and included heat transfer and solidification. This model is described in the next section.

3. MATHEMATICAL MODEL

3.1. Fluid Flow and Free Surface Reconstruction

We begin a discussion of our model by introducing a few simplifying assumptions. We assume that for the impact of a droplet against a solid surface, that the surrounding gas about the droplet is dynamically inactive, which implies that the impact may be modeled by following the flow field only in the liquid phase. The droplet is assumed to be spherical at impact. The liquid is modeled as incompressible. Fluid flow is assumed to be Newtonian and laminar. And, finally, as a consequence of these assumptions, we assume that the only stress at the liquid free surface is a normal stress, and that any tangential stress is negligible.

Equations of conservation of mass and momentum govern the fluid dynamics:

$$\nabla \cdot \mathbf{V} = 0 \tag{5}$$

$$\frac{\partial \mathbf{V}}{\partial t} + (\mathbf{V} \cdot \nabla)\mathbf{V} = \frac{-1}{\rho}\nabla p + \nu \nabla^2 \mathbf{V} + \frac{1}{\rho}\mathbf{F}_b \tag{6}$$

where $\mathbf{V}$ represents the velocity vector, p the pressure, ρ the density, ν the kinematic viscosity, and $\mathbf{F}_b$ any body forces acting on the fluid.

Boundary conditions for fluid along solid surfaces are the no-slip and no-penetration conditions. At the liquid free surface, Laplace's equation specifies the surface tension-induced jump in the normal stress p_s across the interface

$$p_s = \gamma \kappa \tag{7}$$

where γ represents the liquid–air surface tension and κ the total curvature of the interface.

Finally, a boundary condition is required at the contact line, the line at which the solid, liquid and gas phases meet. It is this boundary condition which introduces into the model information regarding the wettability of the solid surface. Although it is conceivable that one could formulate this boundary condition incorporating values of the solid surface tensions, such values are often inaccessible. Rather, we specify the contact angle, θ, the value of which can be a constant or dependent on the contact line speed.

The basis for our model is RIPPLE,[25] a 2-D fixed-grid Eulerian code written specifically for free surface flows with surface tension. In addition to three-dimensionalization of the code, significant improvements are incorporated into the model, including new algorithms for evaluating surface tension and for interface tracking. We focus on these improvements in what follows. Note that we present some details in a 2-D context to avoid unnecessary complexity.

Equations (1) and (2) are discretized according to typical finite volume conventions on a rectilinear grid encompassing both the volume occupied by the droplet prior to impact as well as sufficient volume to accommodate the subsequent deformation. Velocities and pressures are specified as on a traditional staggered grid[28]: velocities at the center of cell faces, pressure at the cell center (see Fig. 4). Equations (5) and (6) are solved using a two-step projection method, in which a time discretization of the momentum equation is broken up into two steps.[22]

In addition to solving the flow equations within the liquid, the numerical model must also track the location of the liquid free surface. Various approaches exist to tracking a sharp discontinuity through a flow field: the

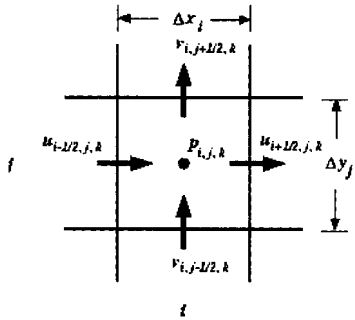

Fig. 4. A 2-D control volume, with velocities specified at cell faces, pressure at the cell center.

approach chosen here is the first-order accurate 3-D volume tracking method of Youngs[29] in place of the Hirt–Nichols algorithm[30] implemented in RIPPLE. Although the Hirt–Nichols algorithm can be three-dimensionalized, Youngs' algorithm is a more sophisticated and more accurate approach. A recent comparison of various 2-D algorithms,[31] including Hirt–Nichols and Youngs' equivalent 2-D method,[32] demonstrated a significant difference in the accuracy of the two approaches.

Consider a function f defined in a continuous domain as

$$f = \begin{cases} 1 & \text{within the liquid phase} \\ 0 & \text{without} \end{cases} \tag{8}$$

For a cell (i, j, k) of volume $v_{i,j,k}$ a "volume fraction" $f_{i,j,k}$ is defined as

$$f_{i,j,k} = \frac{1}{v_{i,j,k}} \int_{v_{i,j,k}} f \, dv, \tag{9}$$

and a corresponding cell density $\rho_{i,j,k}$, which appears in the discretization of Eq. (6), is evaluated as

$$\rho_{i,j,k} = \rho_f f_{i,j,k} \tag{10}$$

where ρ_f represents the (constant) value of the liquid density. Obviously, $f_{i,j,k} = 1$ for a cell filled with liquid and $f_{i,j,k} = 0$ for an empty cell. When $0 < f_{i,j,k} < 1$, the cell is deemed to contain a portion of the free surface and is termed an "interface cell." Note that unlike f, the integrated quantity $f_{i,j,k} = 0$ no longer contains information regarding the exact location of the interface. This is, in fact, the primary drawback of volume tracking as an interface tracking method, and becomes problematic when dealing with surface tension and contact angles. On the other hand, volume tracking is

relatively simple to implement even in three dimensions, retains this simplicity regardless of the complexity of the interface geometry, conserves mass (or volume, since the fluid is incompressible) exactly, and demands only a modest computational resource beyond that required by the flow solver.

Since the function f is passively advected with the flow, f satisfies the advection equation

$$\frac{\partial f}{\partial t} + (\mathbf{V} \cdot \nabla) f = 0 \tag{11}$$

Given the volumetric nature of $f_{i,j,k}$ and in order to maintain a sharp interface, the discretization of Eq. (11) requires special treatment. As with most other volume tracking algorithms, Youngs' algorithm consists of two steps: an approximate reconstruction of the interface followed by a geometric evaluation of volume fluxes across cell faces.

The interface is reconstructed by locating a plane within each interface cell, corresponding exactly to the volume fraction $f_{i,j,k}$ and to an estimate of the orientation of the interface, specfied as a unit normal $\hat{n}_{i,j,k}$ directed into the liquid phase. In two dimensions such an interface is simply a line crossing a cell; in three dimensions the line becomes a three- to six-sided polygon, depending on how the plane slices the cell. To illustrate in two dimensions, Fig. 5b portrays the volume fractions corresponding to the exact (albeit unknown) interface of Fig. 5a. Note that nothing guarantees that interface planes be contiguous. The position of the interface within each cell and the new velocities at the cell faces are then used to determine volume fluxes across each face during the timestep. Figure 5c illustrates such a flux across one face of a cell. Volume fluxes are evaluated one direction at a time,

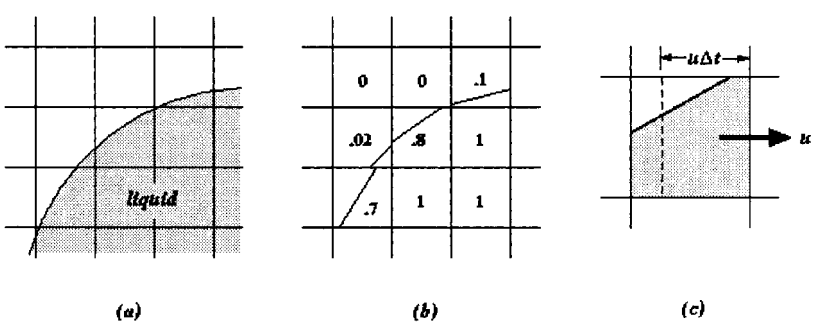

Fig. 5. The volume tracking method in two dimensions. (a) The exact liquid interface. (b) The corresponding volume fractions and planar interfaces. (c) With velocity u positive, the shaded region to the right of the dotted line is advected into the neighboring cell during the time step δt.

always followed by an interim interface reconstruction. Alternating the order of advection from one timestep to the next minimizes directional bias.

The original RIPPLE code was primarily a vehicle for introducing the "Continuum Surface Force," or CSF, model[33] as a novel approach to evaluating surface tension. The CSF model reformulates surface tension into an equivalent volume force $\mathbf{F}_{\mathrm{ST}}$:

$$\mathbf{F}_{\mathrm{ST}}(x) = \gamma \int_S \kappa(\mathbf{r}) n(\mathbf{r}) \delta(\mathbf{x} - \mathbf{r})\, d\mathbf{r} \tag{12}$$

where δ is the Dirac delta function and the integration is performed over some area of free surface S. Surface tension is then incorporated into the flow equations simply as a component of the body force $\mathbf{F}_b$ in Eq. (6). Discretization of Eq. (12) requires an approximation to δ which spreads the surface tension force over fluid in the vicinity of the surface. Unfortunately, the original discretization of Eq. (12) resulted in a surface tension force distribution, which induced spurious fluid motion near free surfaces.[33] Other discretizations of Eq. (12) have been proposed more recently[34,35] and were tested in both two and three dimensions. The accuracy of our simulations improved dramatically when we incorporated these improvements.

What remains is to evaluate $\hat{n}_{i,j,k}$, required by the volume-tracking algorithm to reconstruct the interface, and essential to the accurate evaluation of $F_{\mathrm{ST}_{i,j,k}}$, especially since κ is evaluated as

$$\kappa = -\nabla \cdot \hat{n} \tag{13}$$

In a continuous domain,

$$\hat{n} = \frac{\nabla f}{|\nabla f|} \tag{14}$$

But given the volumetric nature of $f_{i,j,k}$, a simple algebraic discretization of Eq. (14) leads to poor estimates of $\hat{n}_{i,j,k}$. In two dimensions, complex geometric algorithms have been devised to evaluate $\hat{n}$ and κ.[36,37] There are no obvious extensions of these algorithms to three dimensions.

Instead, the approach implemented in our model comes from a suggestion contained within the original CSF formulation.[33] Analogous to spreading the surface tension force to fluid in the vicinity of the free surface, better estimates of $\hat{n}_{i,j,k}$ are obtained by evaluating the gradient of a smoothed $f_{i,j,k}$, equivalent to employing a spatially-weighted gradient operator to evaluate ∇f. In practice, we employ the same δ_{2h} for smoothing $f_{i,j,k}$ as for smoothing $\mathbf{F}_{\mathrm{ST}_{i,j,k}}$. $\hat{n}_{i,j,k}$ is first evaluated at cell vertices, to accommodate the evaluation of the cell-centered $\kappa_{i,j,k}$; cell-centered $\hat{n}_{i,j,k}$ are then evaluated as an average of eight vertex values.

The particular δ_{2h} chosen for the model is a radially symmetric variation of a widely-used kernel proposed by Peskin[38]

$$\delta_{2h}(x) = \begin{cases} \left(1 + \cos\left(\frac{\pi|x|}{2h}\right)\right) \Big/ c & |x| \le 2h \\ 0, & |x| > 2h \end{cases} \tag{15}$$

where c normalizes the kernel

$$c = \tfrac{32}{3} h^3 (\pi^2 - 6)/\pi \tag{16}$$

The reason we modify Peskin's kernel is found in work by Aleinov and Puckett,[34] which demonstrates that radial symmetry appears to be an attractive attribute of δ_{2h}.

Finally, much has been written of the apparent contradiction of a contact line moving along a no-slip solid surface. Analytical solutions of the Navier–Stokes equations yield a force singularity at a contact line unless a slip condition is imposed near the line.[39] Numerical models, which explicitly track the free surface, also require that a slip boundary condition be imposed on any contact line velocities.[40] This turns out not to be an issue for this model, precisely because it does not explicitly track the free surface, nor does it solve for contact line velocities. Instead, since velocities are specified at cell faces, the nearest velocity to the contact line is specified one half-cell height above the solid surface. Again, Fig. 5 provides an illustration. It is then non-zero velocity which is then used to move fluid near the contact line at each timestep.

3.2. Heat Transfer and Solidification

We assume that solidification occurs at melting temperature and neglect viscous dissipation. Densities of liquid and solid are assumed constant and equal to each other. The energy equation can be written as

$$\frac{\partial h}{\partial t} + (\mathbf{V} \cdot \nabla) h = \frac{1}{\rho} \nabla \cdot (k \nabla T) \tag{17}$$

The above equation has two dependent variables: temperature T and enthalpy h. We employed the method of Cao *et al.*[41] to transform the energy equation in terms of enthalpy alone. The main advantage of this method is that it solves the energy equation for both phases simultaneously. The transformed energy equation is as follows[6]:

$$\frac{\partial h}{\partial t} + (\mathbf{V} \cdot \nabla) h = \frac{1}{\rho} \nabla^2 (\beta h) + \frac{1}{\rho} \nabla^2 \phi \tag{18}$$

where in the solid phase

$$h \leq 0; \qquad \beta = \frac{k_s}{C_s}, \qquad \phi = 0 \tag{19a}$$

at the liquid–solid interface

$$0 < h < H_f; \qquad \beta = 0, \qquad \phi = 0 \tag{19b}$$

and in the liquid phase

$$h \geq H_f; \qquad \beta = \frac{k_l}{C_l}, \qquad \phi = -\frac{H_f k_l}{C_l} \tag{19c}$$

where ϕ is a new source term, and H_f is the latent heat of fusion. Subscripts l and s refer to liquid and solid properties, respectively. The energy equation has now only one dependent variable, the enthalpy, h. The relationship between temperature and enthalpy is given by

$$T = T_m + \frac{1}{k}(\beta h + \phi) \tag{20}$$

where T_m is the melting point of the droplet. Heat transfer within the substrate is by conduction only. The governing equation is

$$\rho_w C_w \frac{\partial T_w}{\partial t} = \nabla \cdot (k_w \nabla T_w) \tag{21}$$

where subscript w indicates the substrate. At the free surface, we used an adiabatic boundary condition. Note that, initially, the dominant heat loss from the droplet is due to heat conduction to the substrate and, later on, conduction and convection to the solidified layer. Estimates of heat loss by convection from the droplet surface to the surrounding gas showed that it is three orders of magnitude lower than heat conduction to the substrate. Therefore, the adiabatic condition at the free surface is reasonable. This condition can, however, be easily modified to a convective, radiative, or mixed boundary condition.

3.3. Thermal Contact Resistance

The incomplete contact between the drop and the substrate results in a temperature discontinuity across the contact surface. The effect can be incorporated in the model via definition of the thermal contact resistance, R_c:

$$R_c = \frac{(T - T_w)_{\text{substrate}}}{q} \tag{22}$$

where q is the heat flux from the droplet to substrate. Values of R_c are provided as an input to the model. Although in principle R_c could vary with time and/or position on the interface, we assumed it to be a constant. In our experience, R_c typically varies between 10^{-6} to 10^{-7} m^2 K/W.

3.4. Effect of Solidification on Fluid Flow

Computation of velocity field has to account for the presence of a moving, irregularly shaped solidification front on which the relevant boundary conditions are applied. We treat the solidified regions by a modified version of the fixed velocity method. In this approach, a liquid volume fraction Θ is defined such that $\Theta = 1$ for a cell completely filled with liquid; $\Theta = 0$ for a cell filled with solid; and $0 < \Theta < 1$ for a cell containing a portion of the solidification front. Normal and tangential velocities on the faces of cells containing only solidified material are set to zero. The modified continuity and momentum equations are then given by[42]

$$\nabla \cdot (\Theta \mathbf{V}) = 0 \tag{23}$$

$$\frac{\partial(\Theta \mathbf{V})}{\partial t} + (\Theta \mathbf{V} \cdot \nabla)\mathbf{V} = \frac{-\Theta}{\rho}\nabla p + \Theta \nu \nabla^2 \mathbf{V} + \frac{\Theta}{\rho}\mathbf{F}_b \tag{24}$$

$$\frac{\partial f}{\partial t} + (\Theta \mathbf{V} \cdot \nabla) f = 0 \tag{25}$$

3.5. Numerical Procedure

The modified Navier–Stokes, volume of fluid, and energy equations are solved on an Eulerian, rectangular, staggered mesh in a 3-D Cartesian coordinate system. The computational procedure for advancing the solution through one time step is as follows:

1. From time level n values, the velocity and pressure fields as well as f are calculated at time level $n + 1$ in accordance with the 3-D model of Bussmann *et al.*[22]
2. Given droplet enthalpy and substrate temperature fields at time level n, Eqs. (18) and (21) are solved implicitly to obtain the new enthalpy field in the droplet and the new temperature field in the substrate. Temperatures in the droplet can then be calculated from Eq. (20).
3. New values of the liquid volume fraction Θ are calculated from the enthalpy field in the droplet by using Eq. (19a–c) in conjunction with an algorithm described by Voller and Cross.[43] In this algorithm, as phase change proceeds in a computational cell, the rate of change in the cell enthalpy is the product of the speed of the phase change front and the latent heat of fusion.

4. Flow and thermal boundary conditions are imposed on the free surface, at the solidification front, and other boundaries of the computational domain. In particular, the thermal contact resistance at the droplet–substrate interface is applied by using Eq. (22) and the heat flux to the substrate is calculated. This value of q is then used to update temperature boundary conditions along the bottom surface of the droplet and the uper plane of the substrate.

Repetition of these steps allowed advancing the solution through a given time interval. For the impact of a droplet on an incline with a grid resolution of 20 cells per radius, typical CPU time on a Sun Ultra Enterprise 450 workstation ranged between 70 to 120 hr.

4. RESULTS AND DISCUSSION

Figure 6 shows a variety of splats obtained with atmospheric plasma spraying under different substrate and impact conditions. The droplets may assume a circular shape, or may splash and breakup. Breakup of thermal spray droplets on a smooth substrate occurs when substrate temperature is below a certain value. The temperature at which the splat shape becomes circular is referred to as "transition temperature."[26] Pasandideh-Fard *et al.*[26] investigated the type of instability that breaks up the splat and the role of substrate temperature in this regard.

Figure 7 shows the simulation views of a 73 m/s normal impact of a 60 μm Nickel droplet on a stainless steel substrate at 290°C initial temperature (the figure corresponds to the half volume fraction isosurface). The initial droplet temperature was 1600°C, i.e., 150°C superheat, and the contact resistance was low at $10^{-7}\,\mathrm{m^2\,K/W}$. Considering Nickel properties (Table I), This case corresponds to Re = 7892, We = 1419, Ste = 1.67, and Pr = 0.043; hence, $\sqrt{\mathrm{Ste}/\mathrm{Pr}} = 6.2$, which indicates the effect of solidification on droplet spreading is important.

Immediately following impact, liquid jets out from under the drop and spreads in the radial direction. Solidification is, however, fast enough that all parts of the droplet in contact with the substrate freeze 0.5 μs after impact (see Fig. 8). When the bottom layer is solidified, the remaining liquid jets out over the rim of the splat. We notice that shortly after the impact, the contact line becomes unstable leading to the liquid breakup. The shape of liquid ligaments detached from the bulk of the splat changes due to surface tension effects. During this shape oscillation, most ligaments touch the surface because they move close to the substrate. When this occurs, the liquid is dragged on the substrate (no-slip condition) making a finger around the bulk of the splat (Fig. 7 at 10 μs). Small parts of the detached liquid

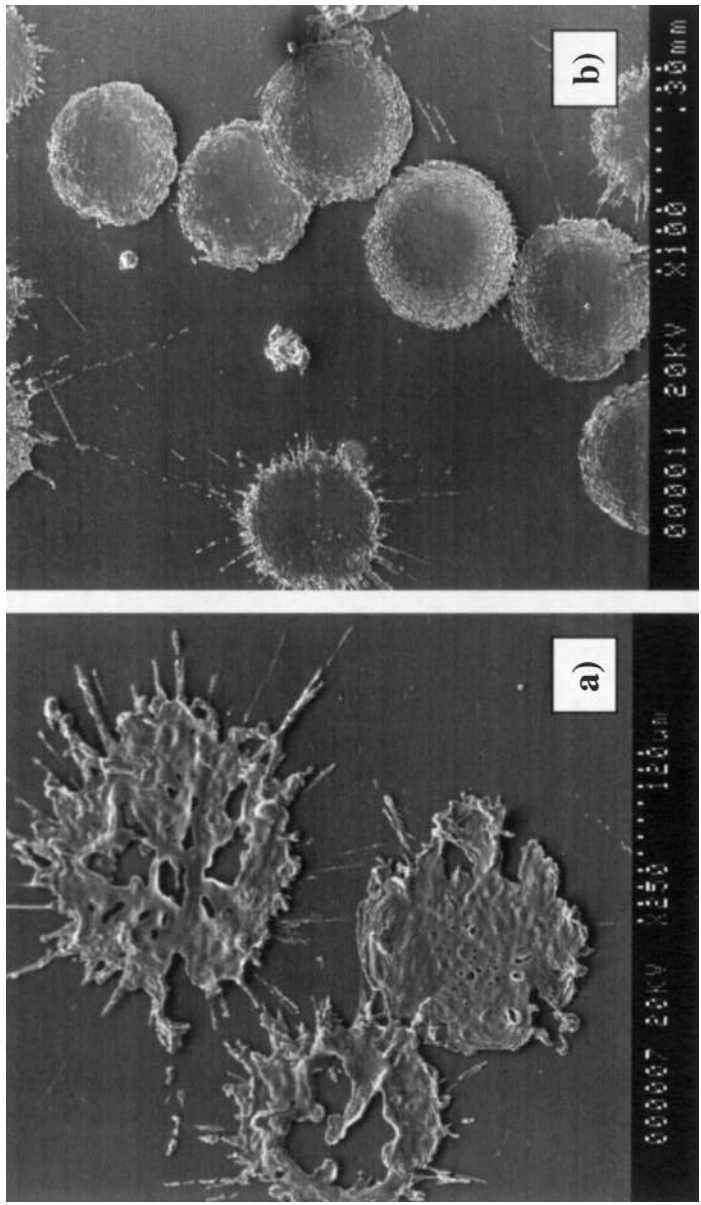

Fig. 6. Nickel splats deposited on a stainless steel surface initially at (a) 290°C and (b) 400°C. Adapted from Ref. 26.

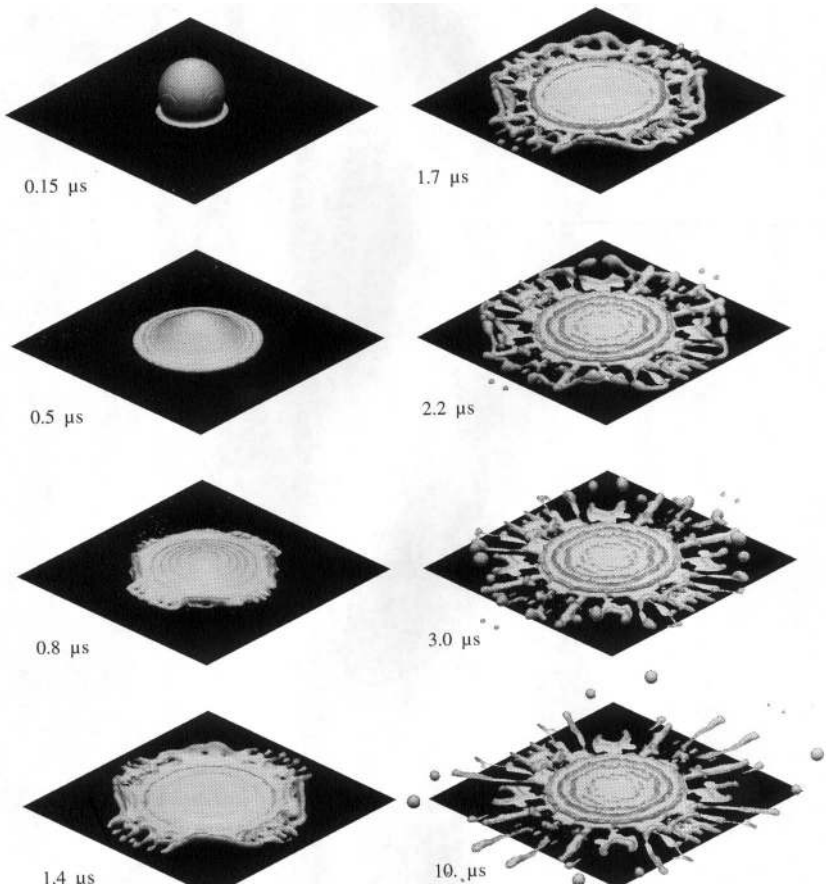

Fig. 7. Simulations showing the impact of a 60 μm diameter molten nickel particle at 1600°C landing with a velocity of 73 m/s on a stainless steel plate initially at a temperature of 290°C. The contact resistance at the substrate surface was assumed to be 10^{-7} m^2 K/W. Adapted from Ref. 26.

that fly away from the splat will eventually come back down due to the effect of gravity. The final shape of the simulated splat resembles the appearance of those observed in our experiments under similar conditions.

In the absence of solidification, Rayleigh–Taylor instability[23] plays the dominant role in the breakup of an impacting droplet. To show that Rayleigh–Taylor instability is not responsible for the breakup described above, and it is in fact solidification that causes splashing, we simulated the above impact without heat transfer and solidification. Results showed no splashing; even when we initially induced formation of fingers, they merged later

Table I. Properties of Nickel, Alumina, and Stainless Steel. For Substrate Material (Stainless Steel) the Only Properties Needed are Density, Thermal Conductivity, and Specific Heat

Material / Properties		Nickel	Alumina	Stainless steel	
Density [kg/m^3]		7.9E3	3.0E3		6.97E3
Melting point [°C]		1453	2050		—
Heat of fusion [J/kg]		3.1E5	1.075E6		—
	°C				
Kinematic viscosity [m^2/s]	1453	6.7E–7	1.026E–5		—
	1477	6.4E–7			
	1527	6.0E–7			
	1577	5.7E–7			
	1627	5.4E–7			
	1727	5.0E–7			
Liquid thermal conductivity [W/(m K)]		45	6		—
Liquid specific heat [J/(kg K)]		444	1300		—
Surface tension [N/m]		1.78	0.69		—
	°C			°C	
Solid thermal conductivity [W/(m K)]	527	67.6	6	127	16.6
	727	71.8		327	19.8
	927	76.2		527	22.6
	1227	82.6		727	25.4
				927	28.0
				1227	31.7
	°C			°C	
Solid specific heat [J/(kg K)]	527	530	1273	127	515
	727	562		327	557
	927	594		527	582
	1227	616		727	611
				927	640
				1227	682

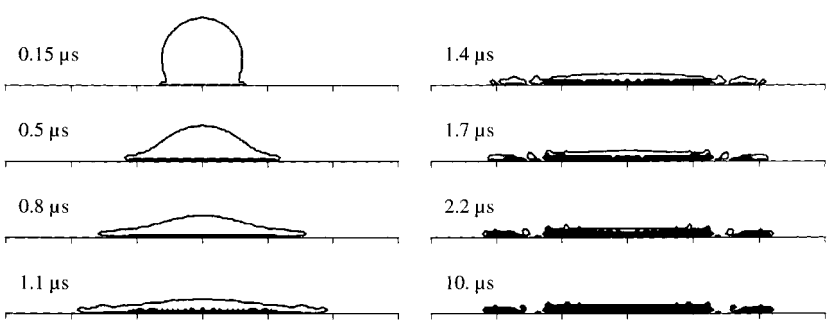

Fig. 8. A cross-sectional view of the images in Fig. 5. Black shows the solidified portion of the droplet and white represent liquid. Adapted from Ref. 26.

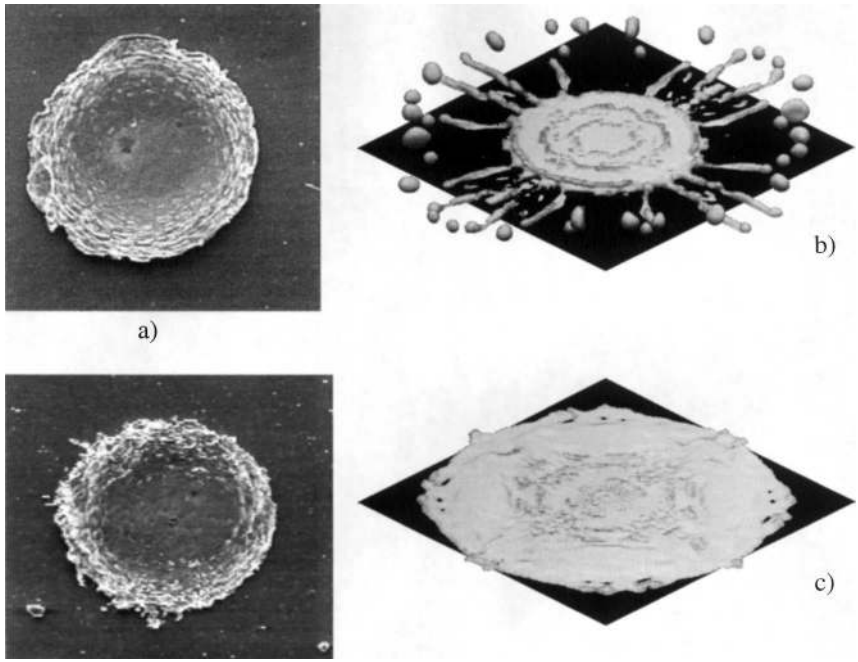

Fig. 9. Nickel splat shapes on a steel plate initially at 400°C from (a) experiments (b) numerical model assuming a contact resistance of $10^{-7}\,m^2\,K/W$ and (c) numerical model assuming a contact resistance of $10^{-6}\,m^2\,K/W$. Adapted from Ref. 26.

on and the final shape was circular. Extensive trials with the numerical model confirmed that solidification is necessary to trigger splashing in a nickel droplet of the size used in thermal spray coatings (<100 μm).

To model the effect of substrate temperature on final splat shape, we increased the initial substrate temperature to 400°C. Figure 9a shows two images of disk splats that we collected after spraying a stainless steel surface initially at 400°C. Figure 9b shows the final shape of our simulated splat, calculated assuming an initial surface temperature of 400°C and a thermal contact resistance $R_c = 10^{-7}\,m^2\,K/W$. The droplet showed less splashing than it did in the previous simulation of impact on a surface at 290°C (see Fig. 7), but there are still a significant number of fingers around it. The reason splashing diminishes on a hotter surface is that solidification is delayed and therefore the fluid flow is not disturbed as much by a thinner frozen layer. In other words, increasing the substrate temperature reduces Stefan number, while Prandtl number remains unchanged. As was stated before the ratio of Stefan number to Prandtl number reflects the importance of solidification effect on spreading.

Splashing could be eliminated completely in our simulations if the droplet did not start solidifying until it had finished spreading. The onset of solidification could be delayed if we increased the value of the thermal contact resistance between the drop and the substrate, thereby reducing heat transfer. Figure 9c shows the final splat shape on a surface at a temperature of 400°C assuming a thermal contact resistance $R_c = 10^{-6}\,\mathrm{m^2\,K/W}$, which is an order of magnitude larger than that used previously. The splat was disk shaped, with no splashing, looking much like those observed experimentally (Fig. 9a). The increase in thermal contact resistance is expected, since raising stainless steel substrate temperature thickens the surface oxide layer, hence increasing thermal contact resistance. The measurement of oxide layer thickness has confirmed this statement.[26] These results agree well with the previous study of Fukomoto, Huang, and Ohwatari,[44] who also observed a sharp transition from splashing to disk splats when spraying nickel particles on stainless steel.

Solidification inside a spreading droplet can trigger splashing. However, other protrusions on the surface can also make a droplet splash, such as scratches on the surface.[44] The presence of an already solid splat under an impacting droplet can also create an instability that causes droplet splashing. Figure 10 shows simulations of the sequential impact of two nickel droplets, both 60 μm in diameter and with impact velocities of 48 m/s landing on a stainless steel surface at 194°C. The second droplet landed 5 μs after the first, with its center offset by 140 μm from that of the first droplet. Contact resistance was assumed to be $5 \times 10^{-7}\,\mathrm{m^2\,K/W}$. The first droplet landed, spread, and solidified without any significant splashing, forming a disk splat. The second droplet, introduced after the first one was completely solidified, landed near the edge of the first splat. The spreading sheet of liquid hit the solidified splat and was in part directed sideways; the remainder of the liquid sheet jetted upward over the previously deposited splat and fragments with small droplets flying on top of the splats. We saw evidence of this type of behavior in our experiments: Fig. 11 shows two splats deposited next to each other on a surface at 400°C. The first splat is disk like, but the second splashed after hitting the edge of the first. Streaks of splashed material are visible on the surface of the first splat.

Droplet and substrate materials properties are obviously important in determining the splat shapes. Recently, Pershin *et al.*[45] studied both experimentally and numerically, the effect of substrate temperature on alumina splat shapes. Two substrate materials, glass and stainless steel, were employed. As shown in Table I, Alumina and Nickel have substantially different properties. Compared to Nickel, Alumina is substantially more viscous, less dense, has higher melting point temperature and higher heat of fusion, as well as much larger specific heat.

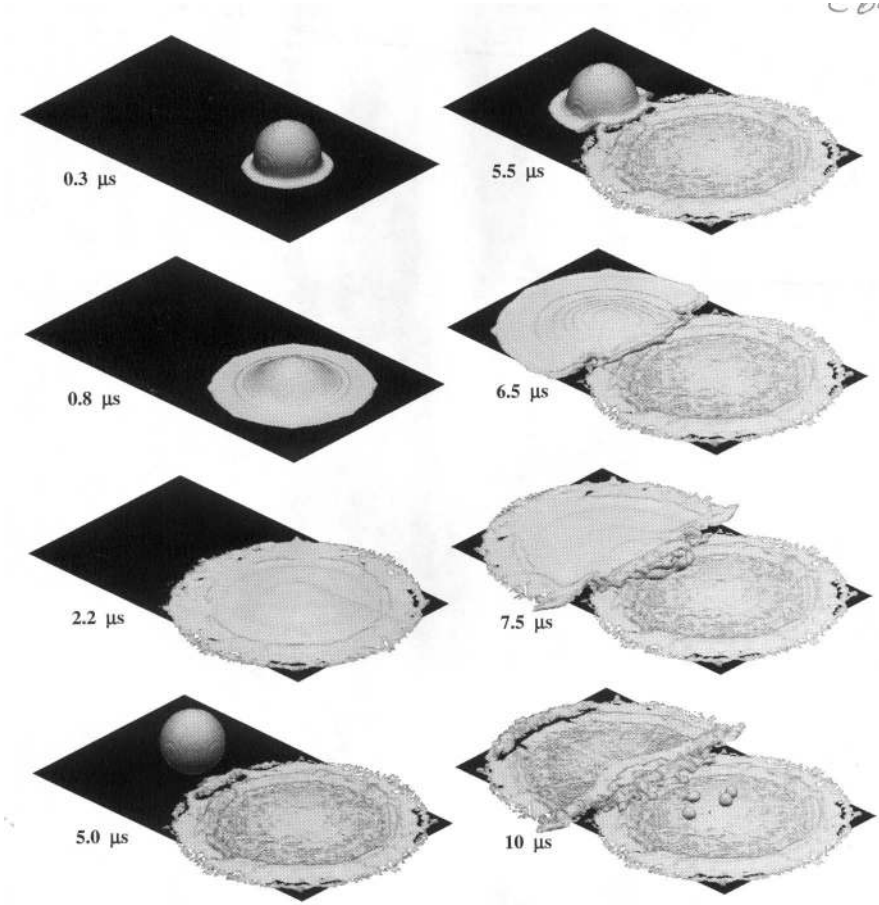

Fig. 10. Simulation images of the impact of two nickel particles (60 μm diameter; 48 m/s impact velocity; initial temperature 2050°C) on a stainless steel substrate initially at a temperature of 194°C. The contact resistance below the droplets was assumed to be 5×10^{-7} m^2 K/W. Adapted from Ref. 26.

Figure 12 shows the predicted splat shape for the case of a 25-μm, 2260°C alumina droplet impacting normally at 105 m/s on a stainless steel substrate initially at 25°C (Fig. 12a) and 500°C (Fig. 12b). No breakup is predicted. The non-dimensional parameters for this case are: Re = 267.5; We = 1198; Pr = 6.67; and Ste = 2.7 (for 25°C) and 2.13 (for 500°C). Thus, for both substrate temperatures, $\sqrt{\text{Ste}/\text{Pr}} < 1$ and solidification does not play a significant role on droplet spreading. In addition, for the given conditions, Rayleigh–Taylor instability does not cause break-up. Hence, in the

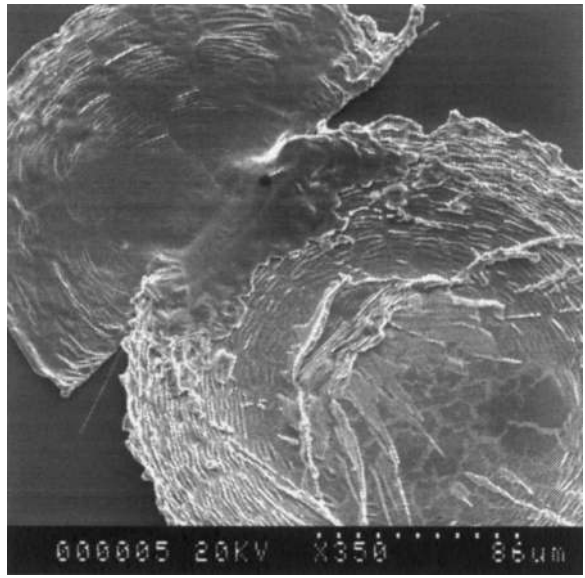

Fig. 11. Micrograph of two nickel particles deposited on a stainless steel surface at 400°C. Adapted from Ref. 26.

case of atmospheric sprayed alumina, break-up seems to occur considerably less that Nickel, or perhaps other metals. Pershin *et al.*,[45], however, report that a minority of alumina droplets breakup when substrate is at room temperature. Figure 13 shows an example of these breakups. The figure suggests that the nature of this break-up is different than that for nickel; there is no particular pattern to it or any symmetry. Presently, our model cannot account for this behavior. We suspect that, in this case, breakup is related to the substrate contamination, which can considerably alter contact angle and wettability. Alumina might be more sensitive to a contamination

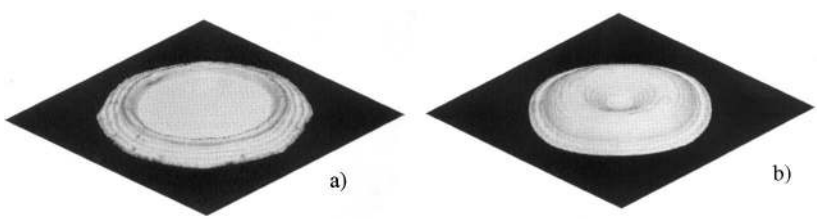

Fig. 12. Final shapes of a 25 μm alumina particle at 210°C above melting point following its 105 m/s impact on a stainless steel plate initially at a temperature of (a) 25°C and (b) 500°C. Adapted from Ref. 45.

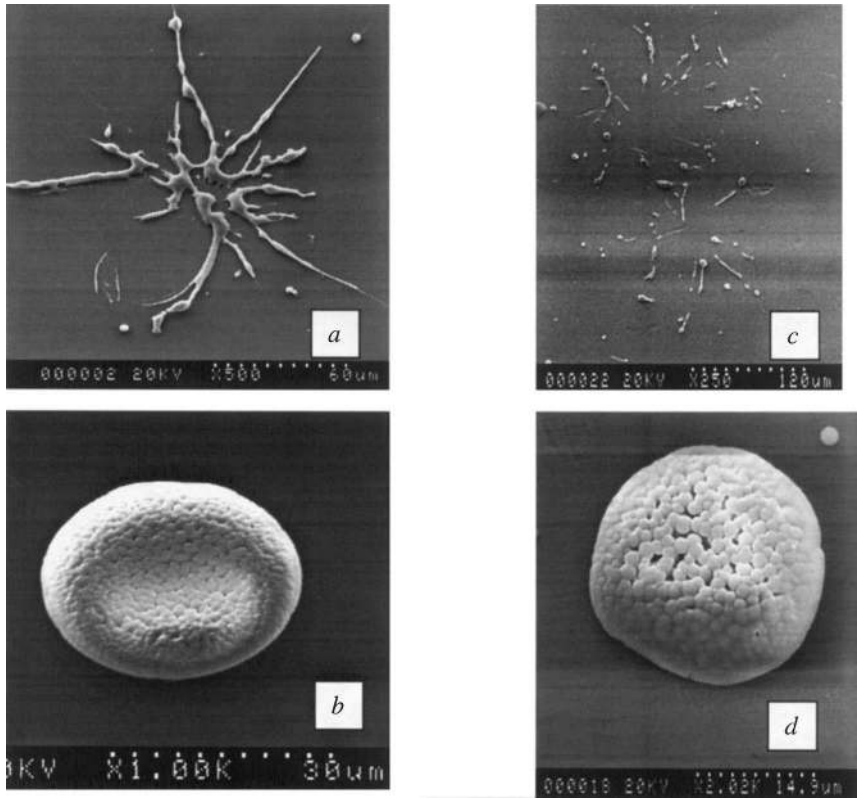

Fig. 13. Two types of alumina splats on glass (a, b) and stainless steel (c, d) substrates at 20°C. Adapted from Ref. 45.

than nickel. It is likely that when substrate temperature is raised, the contamination evaporates, and a clean surface results. Finally, please note that, in the absence of contact angle information, we used a constant contact angle of 90° for all these simulations.

5. CONCLUSIONS AND FUTURE NEEDS

Modeling plasma sprayed splats involves calculation of three-dimensional flow and temperature fields both within the impacting droplet and the substrate. The flow model developed by Bussmann *et al.*[22,23] and extended to include heat transfer and solidification by Pasandideh-Fard *et al.*[26,27] appear to predict droplet impact and solidification accurately for

both metallic and ceramic drops. In addition, the model can simulate multi-droplet impact and investigate their interactions. It was shown that the major reason for splashing, under conditions typical of plasma spray, is indeed solidification. When solidification is slow in comparison with spreading time, no splashing occurs. The importance of solidification on spreading and splashing can conveniently be measured by $\sqrt{\mathrm{Ste}/\mathrm{Pr}}$; when this term is much smaller than unity, solidification does not affect spreading.

There are a number of issues that remain unresolved and are subject of ongoing research. These are listed below:

1. Effect of gas flow about the impacting droplet, which as shown by Mehdi-Nejad *et al.*[46] could result in gas entrapment and formation of a bubble under the impacting droplet.
2. Effect of density change due to solidification; which is the reason for splat curl-up and residual stress. Consideration of this effect is not straightforward as it affects the volume of fluid equation.
3. Development of a model for prediction of thermal contact resistance; the results demonstrate the important effect of thermal contact resistance on final shape of splats. Presently, thermal contact resistance is assumed to be known and its value is estimated by comparing the final splat shapes with experiments.
4. Undercooling effects: Solidification has been assumed to occur under thermal equilibrium conditions, i.e., at droplet melting temperature. The validity of this assumption depends on the heat flux rate to the substrate. It is shown by Chae *et al.*[47] that undercooling can affect the spread ratio.

REFERENCES

1. Y. C. Lee and E. Pfender, *Plasma Chem. Plasma Process.* **7**, 1 (1987).
2. R. Ghafouri-Azar, J. Mostaghimi, and S. Chandra, *Proceedings of the International Thermal Spray Conference*, Singapore, May 2001, pp. 951–958.
3. J. Madejski, *Int. J. Heat Mass Transfer* **19**, 1009 (1976).
4. J. Madejski, *Int. J. Heat Mass Transfer* **26**, 1095 (1983).
5. M. Pasandideh-Fard, Y. M. Qiao, S. Chandra, and J. Mostaghimi, *Phys. Fluids* **8**, 650 (1996).
6. M. Pasandideh-Fard, R. Bhola, S. Chandra, and J. Mostaghimi, *Int. J. Heat Mass Transfer* **41**, 2929 (1998).
7. Z. Zhao, D. Poulikakos, and J. Fukai, *Int. J. Heat Mass Transfer* **39**, 271 (1996).
8. Ibid, *Int. J. Heat Transfer* **39**, 2791 (1996).
9. T. Bennet and D. Poulikakos, *J. Mat. Sci.* **29**, 2025 (1994).
10. B. Khang, Z. Zhao, and D. Poulikakos, *ASME J. Heat Transfer* **116**, 436 (1994).
11. H. Liu, E. J. Lavernia, and R. Rangel, *J. Phys. D: Appl. Phys.* **26**, 1900 (1993).
12. M. Bertagnolli, M. Marchese, and G. Jacucci, *J. Thermal Spray Tech.* **4**, 41 (1995).
13. G. Trapaga, E. F. Mathys, J. J. Valencia, and J. Szekely, *Metallurgical Transactions B* **23B**, 701 (1992).

14. M. Pasandideh-Fard and J. Mostaghimi, *Plasma Chem. Plasma Process.* **16S**, 83S (1996).
15. S. Inada, *J. Chem. Engng Japan* **21**, 582 (1988).
16. T. Watanabe, I. Kuribayashi, T. Honda, and A. Kanzawa, *Chem. Engng Sci.* **47**, 3059 (1992).
17. H. Fukanuma and A. Ohmori, *Proceedings of the 7th National Thermal Spray Conference* pp. 563 (1994)
18. S. Inada and W.-J. Yang, *Experimental Heat Transfer* **7**, 93 (1994).
19. W. Liu, G. X. Wang, and E. F. Matthys, *Int. J. Heat Mass Transfer* **38**, 1387 (1995).
20. A. M. Worthington, *Proc. R. Soc. London* **25**, 498 (1876).
21. A. M. Worthington, in *The Splash of a Drop*, The Society for Promoting Christian Knowledge, London (1907).
22. M. Bussmann, J. Mostaghimi, and S. Chandra, *Phys. Fluids* **11**, 1406 (1999).
23. M. Bussmann, S. Chandra, and J. Mostaghimi, *Phys. Fluids* **12**, 3121 (2000).
24. M. Bussmann, *Ph.D. Thesis*, Department of Mechanical and Industrial Engineering, University of Toronto (1999).
25. D. B. Kothe, R. C. Mjolsness, and M. D. Torrey, *Technical Report*, *LA-12007-Ms*, Los Alamos National Laboratory (1991).
26. M. Pasandideh-Fard, V. Pershin, S. Chandra, and J. Mostaghimi, *J. Thermal Spray Technology* (2000) (submitted).
27. M. Pasandideh-Fard, S. Chandra, and J. Mostaghimi, *1st International Thermal Spray Conference*, Montreal, Quebec pp. 125 (2000)
28. S. V. Patankar, *Numerical Heat Transfer and Fluid Flow*, McGraw-Hill, New York (1980).
29. D. L. Youngs, *Technical Report 44/92/35*, AWRE (1984).
30. C. W. Hirt and B. D. Nichols, *J. Comput. Phys.* **39**, 201 (1981).
31. M. Rudman, *Int. J. Numer. Methods Fluids* **24**, 671 (1997).
32. D. L. Youngs, *Numerical Methods for Fluid Dynamics*, Academic Press, New York (1982), pp. 273.
33. J. U. Brackbill, D. B. Kothe, and C. Zemach, *J. Comp. Phys.* **100**, 335 (1992).
34. I. Aleinov and E. G. Puckett, *Proceedings of the 6th International Symposium on Computational Fluid Dynamics,* Lake Tahoe, CA (1995), pp. 13.
35. D. B. Kothe, W. J. Rider, S. J. Mosso, J. S. Brock, and J. I. Hochstein, *Technical Report 96-0859*, AIAA (1996).
36. A. J. Chorin, *J. Comput. Phys.* **57**, 472 (1985).
37. J. Y. Poo and N. Ashgriz, *J. Comput. Phys.* **84**, 483 (1989).
38. C. S. Peskin, *J. Comput. Phys.* **25**, 220 (1977).
39. E. B. Dussan V and S. H. Davis, *J. Fluid Mech.* **65**, 71 (1974).
40. J. Fukai, Y. Shiiba, T. Yamamoto, O. Miyatake, D. Poulikakos, C. M. Megaridis, and Z. Zhao, *Phys. Fluids* **7**, 236 (1995).
41. Y. Cao, A. Faghri, and W. S. Chang, *Int. J. Heat Mass Transfer* **32**, 1289 (1989).
42. M. Pasandideh-Fard, *Ph.D. Thesis*, Department of Mechanical and Industrial Engineering, University of Toronto, Toronto, Canada (1998).
43. V. Voller and M. Cross, *Int. J. Heat Mass Transfer* **26**, 147 (1983).
44. M. Fukomoto, Y. Huang, and M. Ohwatari, *Proceedings of the 15th International Thermal Spray Conference*, Prague, Czech Republic (1998) pp. 410.
45. V. A. Pershin, M. Pasandideh-Fard, J. Mostaghimi, and S. Chandra, *Proceedings of the International Thermal Spray Conference*, Singapore, May 2001, pp. 813–820.
46. V. Mehdi-Nejad, J. Mostaghimi, and S. Chandra, *8th CFD Society of Canada*, Montreal, Quebec (2000) pp. 567.
47. Y. K. Chae, J. Mostaghimi, and T. Yoshida, *Journal of Science and Technology of Advanced Materials* **1**, 147 (2000).